

Effect of preheat temperature and post-process treatment on the microstructure and mechanical properties of stainless steel 410 made via ultrasonic additive manufacturing

Tianyang Han^a, Chih-Hsiang Kuo^b, Niyanth Sridharan^{b,c}, Leon M. Headings^a, Sudarsanam Suresh Babu^{b,c}, Marcelo J. Dapino^{a,*}

^a Center for Ultrasonic Additive Manufacturing, Department of Mechanical and Aerospace Engineering, The Ohio State University, Columbus, OH, 43210, USA

^b Department of Mechanical, Aerospace, and Biomedical Engineering, University of Tennessee, Knoxville, TN, 37996, USA

^c Oak Ridge National Laboratory, Oak Ridge, TN, 37830, USA

ARTICLE INFO

Keywords:

Ultrasonic additive manufacturing
Stainless steel
Shear test
Hot isostatic pressing
Recrystallization
Electron backscatter diffraction

ABSTRACT

Ultrasonic additive manufacturing (UAM) is a solid-state manufacturing technology for producing near-net shape metallic parts combining additive ultrasonic metal welding and subtractive machining. Even though UAM has been demonstrated to produce robust metal builds in Al–Al, Al–Ti, Al–steel, Cu–Cu, Al–Cu, and other material systems, UAM welding of high strength steels has proven challenging. This study investigates process and post-processing methods to improve UAM steel weld quality and demonstrates the UAM fabrication of stainless steel 410 (SS 410) builds which possess, after post-processing, mechanical properties comparable with bulk material. Unlike UAM fabrication of softer metals, this study shows that increasing the baseplate temperature from 38°C (100°F) to 204°C (400°F) improves interfacial strength and structural homogeneity of the UAM steel samples. Further improvement in strength is achieved through post-processing. The hot isostatic pressing (HIP) post treatment improves the shear strength of UAM samples to 344 MPa from 154 MPa for as-welded samples. Microstructural analyses with SEM and EBSD show no evidence of body centered cubic (BCC) ferrite to face centered cubic (FCC) austenite transformation taking place during UAM welding of SS 410. The weld quality improvement of UAM steel at higher baseplate temperatures is believed to be caused by the reduction of the yield strength of SS 410 at elevated temperature. HIP treatment is shown to increase the overall hardness of UAM SS 410 from 204 ± 7 HV to 240 ± 16 HV due to the formation of local pockets of martensite. Nanohardness tests show that the top of layer n is harder than the bottom of layer $n+1$ due to grain boundary strengthening.

1. Introduction

Ultrasonic additive manufacturing (UAM), also known as ultrasonic consolidation, is a solid-state manufacturing process that combines additive welding and subtractive machining [6]. During the welding process, a rolling sonotrode is used to apply a force normal to metal foil feedstock along with ultrasonic (20 kHz) transverse vibrations. The resulting localized plastic deformation has the effect of collapsing asperities and dispersing oxides and contaminants at the welding interface, generating nascent metal surfaces that produce gapless metallurgical bonds. UAM welding typically occurs at temperatures that are less than one half of the melting temperature of the constituent materials [14]. This enables dissimilar material combinations, such as

Al–Ti [25,32] and Al–ceramic [3], to be achieved by UAM without the creation of brittle phases. The welding process is then repeated to build a component. A computer numerical control (CNC) stage is employed to selectively remove material and machine the part to final dimensions. The subtractive stage can also be used to make arbitrary internal features such as channels and cavities for embedding reinforcement fibers [7,30] and thermally sensitive materials like nickel titanium shape memory alloys [9,10] and fiber optics [20]. A schematic of the UAM process is shown in Fig. 1.

UAM has been proven to produce robust similar metal builds in Al–Al [12,23,31] and Cu–Cu [26] material systems. However, UAM welding of high strength steel remains challenging. In the early stages of research on UAM welding of steel, Tuttle [28] showed that it is possible to weld

* Corresponding author.

E-mail address: dapino.1@osu.edu (M.J. Dapino).

<https://doi.org/10.1016/j.msea.2019.138457>

Received 31 January 2019; Received in revised form 21 August 2019; Accepted 25 September 2019

Available online 28 September 2019

0921-5093/© 2019 Elsevier B.V. All rights reserved.

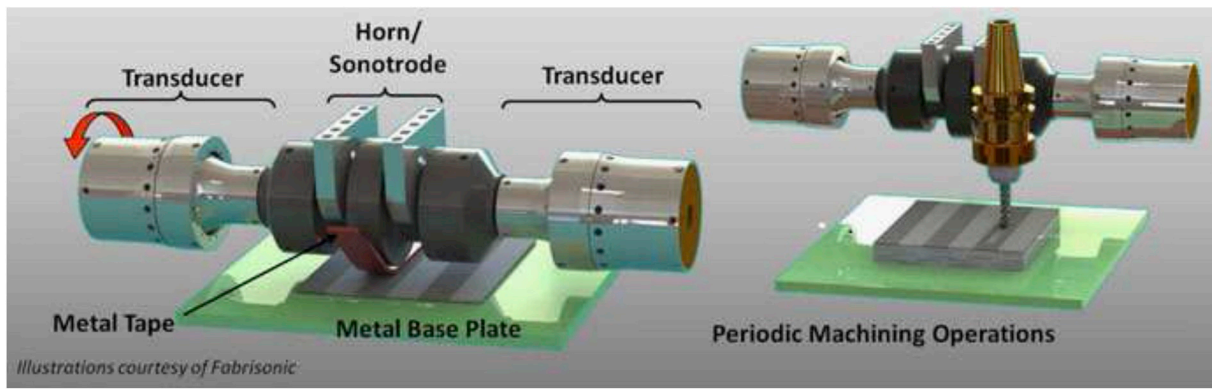


Fig. 1. Schematic of the UAM process.

AISI austenitic stainless steel 316L (SS 316L) foil to a baseplate. However, no foil-to-foil bonding was achieved and optical images of the foil-to-baseplate interface showed that the foil was only partially bonded to the baseplate. Gonzalez et al. [5] used thinner SS 316L foils to achieve steel foil-to-foil bonding via UAM and identified the optimum parameter set for welding SS 316L based on optical images and linear weld density. However, no mechanical properties of UAM-fabricated SS 316L builds were provided in this research. These UAM steel studies included no post-process treatment methods. For UAM, post-process treatment methods like hot isostatic pressing (HIP) have been shown to be beneficial for improving the weld quality of UAM builds [8,15]. In a recent study by Asaf et al. [15], spark plasma sintering (SPS) and HIP have been applied to UAM-made AISI carbon steel 4130 steel samples to further improve the mechanical properties and microstructural homogeneity. Shear testing and microstructural analyses were conducted and reported. The results show that both treatments improve the weld quality of UAM builds, but the SPS method also introduces carbon into the material and thus varies the material homogeneity in the z-direction. The effect of UAM process parameters on steel builds is not presented. In a recent study by Kuo et al. [16], a method to achieve a steel-steel weld with UAM was proposed. The concept is to use soft Ni interlayers between the steel layers and then dissolve the Ni into the steel with a post weld heat-treatment. However, this study indicates that the Ni interlayer must have a thickness less than 10 μm to completely dissolve in the steel and form a steel-steel bonding interface.

These studies have shown the promise of UAM to print high strength steel parts and indicate that a potential improvement of weld quality may be achieved by applying heat input and post-process treatment to the UAM-fabricated steel builds. In this paper, the weldability of AISI martensitic stainless steel 410 (SS 410) along with the effect of pre-heat baseplate temperature and post-process HIP on the mechanical properties and microstructure of UAM-fabricated SS 410 are studied. Even though different preheat temperatures were shown to not have a significant impact on the bond quality of UAM structures in a design of experiments study on Al alloys [31], there is evidence that preheat temperature may be beneficial for steel welding [5,28]. Thus, varied pre-heat temperatures are used in this study to investigate their effect on UAM steel weld quality. Furthermore, the influence of HIP as a post-process method to improve mechanical and microstructural properties of UAM steel builds is investigated. A customized shear test was designed to test the mechanical strength of UAM samples that were built under different conditions. The shear strength of UAM-fabricated SS 410 was benchmarked against bulk SS 410. Optical microscope, scanning electron microscope (SEM) and electron backscatter diffraction (EBSD) analyses, as well as microindentation and nanoindentation tests, were used to gain deeper insights into the effect of the UAM process on the microstructure and hardness of weld interfaces and bulk material.

Table 1
Process parameters used for SS 410 weld.

Parameters	Level 1	Level 2
Normal force (N)	6000	6000
Vibration amplitude (μm)	31.08	31.08
Weld speed (m/s)	0.017	0.017
Baseplate temperature ($^{\circ}\text{C}$)	38	204

Table 2
Test plan.

Pre-heat Temperature	As-welded	HIP
38 $^{\circ}\text{C}$ (100 $^{\circ}\text{F}$)	Shear	Shear
204 $^{\circ}\text{C}$ (400 $^{\circ}\text{F}$)	Shear/SEM/EBSD	Shear/SEM/EBSD

2. Experimental methods

2.1. Sample fabrication and test plan

In this study, all samples were manufactured using a Fabrisonic SonicLayer 4000 9 kW UAM system. Nine layers of 0.127 mm (0.005 in) thick, 25.4 mm (1 in) wide annealed SS 410 steel foils¹ were automatically fed and welded onto a 12.7 mm (0.5 in) thick ASTM A36 hot-rolled carbon steel baseplate.

Pilot welds were performed to identify viable weld parameters; those include normal force, vibration amplitude, weld speed, and baseplate preheat temperature. As is common practice in UAM work, weld parameters were considered viable when a welded foil could not be pulled off by hand. A baseplate temperature of 38 $^{\circ}\text{C}$ (100 $^{\circ}\text{F}$) is the lowest temperature at which UAM SS 410 can be successfully welded within the process window. A baseplate temperature of 204 $^{\circ}\text{C}$ (400 $^{\circ}\text{F}$) is the recommended upper limit for commercial UAM machines. The process parameters and levels that are selected for building UAM samples in this study are listed in Table 1.

Four different treatment combinations were utilized as shown in Table 2. Mechanical shear testing utilizing a custom shear fixture was conducted on all samples. SEM and EBSD analyses were also employed on samples that were welded at a baseplate temperature of 204 $^{\circ}\text{C}$ (400 $^{\circ}\text{F}$) to be tested for both as-welded and HIP treatment conditions.

2.2. HIP processing

One UAM SS 410 build for each weld condition was treated under HIP. Typical HIP systems deliver up to 2000 $^{\circ}\text{C}$ temperature and up to

¹ The welding width of the sonotrode is 20.3 mm (0.8 in).

Table 3

Process parameters selected for HIP UAM SS 410.

Hold Temperature	Hold Pressure	Hold Time	Atmosphere
1121°C	103.42 MPa	4 h	Argon

207 MPa pressure [19]. The process parameters summarized in Table 3 were determined based on previous HIP studies on similar materials like carbon steel 4130 [16] and composite TiB-SS 316L [1]. After HIP treatment, the mechanical properties of the builds were examined by shear testing and the microstructural characteristics were investigated by SEM and EBSD analyses as outlined in Table 2.

2.3. Shear testing

Since the UAM fabricated builds have a unique laminated construction, quantification of the interfacial strength between layers is critical. In previous work, peel testing [13] and push pin testing [34] have been used to provide comparative interfacial strength information. However, these tests cannot provide material properties to benchmark against solid material. Hence a custom shear test method was developed to characterize the mechanical strength of a specific interface of UAM builds. A schematic of the shear fixture is shown in Fig. 2 (a). The use of this type of shear test on UAM samples was first introduced by Wolcott et al. [32].

As presented in Fig. 2(b), a stepped sample geometry has been employed in this study to ensure that the shear occurs at the interface between the baseplate and the first layer of foil. The stepped shear samples were loaded into the fixture and then tested on an MTS C43.504

50 kN load frame. A schematic of the loading condition and an image of the experimental setup are shown in Fig. 2(c)–(d). The tests were conducted on three samples for each weld and treatment condition.

The shear strength is defined as $\tau = F/A$, where F is the maximum compressive force on the fixture during the shear test process that is read from the load frame and A is the cross-sectional area of the sample loaded in shear, which is measured with a micrometer.

2.4. Microstructural analyses

Microstructural analyses including optical imaging, SEM, EBSD, microindentation, and nanoindentation were performed to investigate the global and local changes in microstructure and hardness of UAM samples. In order to preserve the microstructures developed during the UAM and HIP process, samples were sectioned using a low-speed saw with coolant to minimize heating. Then, the samples were mounted in conductive bakelite and polished according to standard metallography preparation procedures. A final polish was performed using colloidal silica to remove the deformed layer on the surface of EBSD samples. Vilella's reagent was used to etch SEM and optical imaging samples. EBSD was performed using a JEOL 6500 machine equipped with an EBSD detector, SEM was performed using a Zeiss EVO MA15 at 20 kV, and optical imaging was performed using a Leica DM4000 M to investigate the microstructure changes due to the UAM and HIP processes. Microindentation tests were carried out with a LECO LM100 to quantify global hardness properties of the UAM steel samples. Nanoindentation tests were performed with an Inforce 1000 machine to obtain local hardness properties across UAM interfaces.

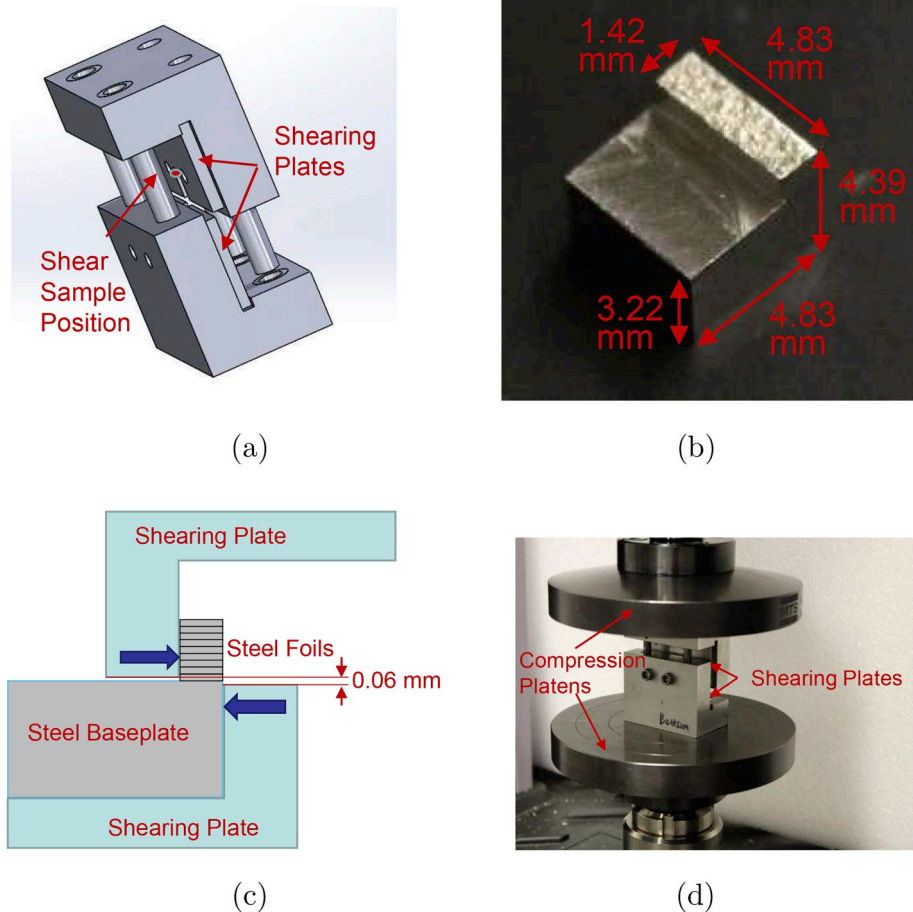


Fig. 2. Shear test design including (a) conceptual schematic of shear fixture, (b) image of stepped shear sample with nominal dimensions, (c) schematic of test loading condition, and (d) experimental setup of the shear test with loaded sample.

Table 4

Average ultimate shear strength of UAM-made SS 410.

Baseplate Temperature	38 °C		204 °C	
Treatment	As-welded	HIP	As-welded	HIP
Shear Strength (MPa)	137.51	337.80	154.22	344.39
Standard Dev. (MPa)	21.99	64.43	13.57	2.28

3. Results

3.1. Shear test results

A summary of the shear test results for all four treatment conditions

is provided in Table 4. Individual loading curves are presented in Fig. 3. Three samples were intended to be tested for each condition. However, one as-welded sample for each baseplate temperature condition failed during machining. No loading curves were obtained for those two samples. As shown, for samples that were welded at a baseplate temperature of 38 °C, the shear strength of HIP treated samples is 337.80 MPa compared with a shear strength of 137.51 MPa for as-welded samples. Similarly, for samples that were welded at a baseplate temperature of 204 °C, HIP treatment more than doubles the shear strength. The average shear strength of HIP/204 °C samples is 344 MPa, which falls in the nominal shear strength range of annealed bulk SS 410 of 330 MPa–470 MPa. These results suggest that the HIP process significantly increases the mechanical strength of the bonding interface.

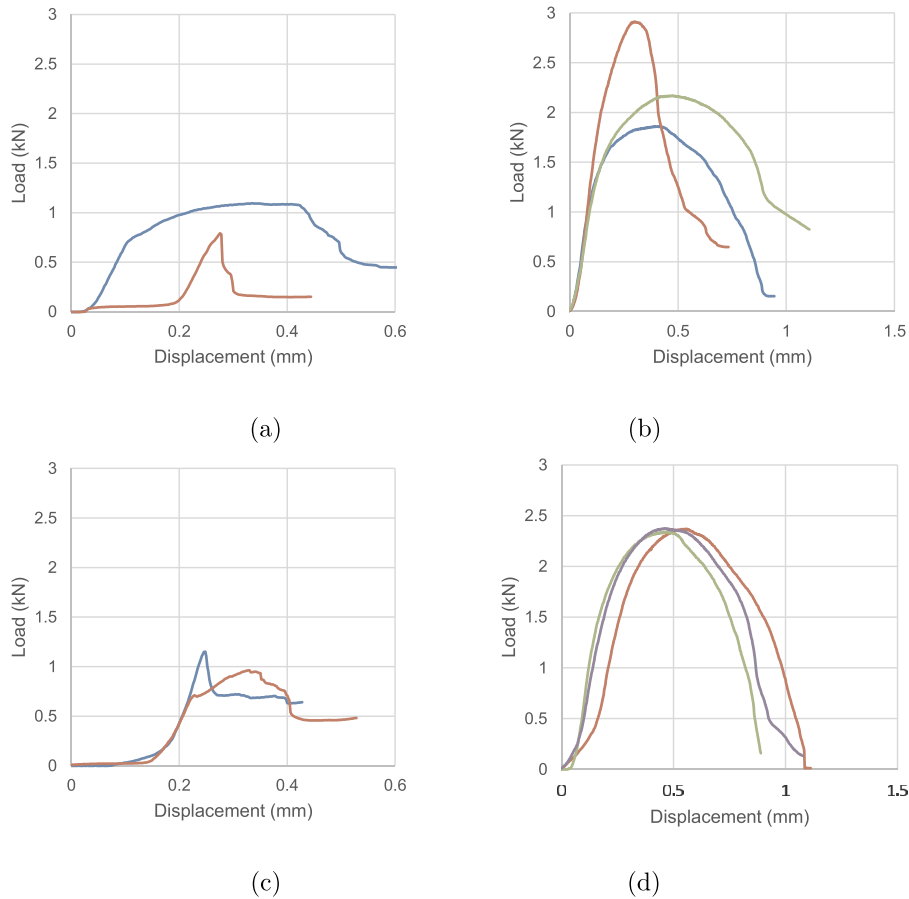


Fig. 3. Shear test results for (a) as-welded/38 °C, (b) HIP/38 °C, (c) as-welded/204 °C, and (d) HIP/204 °C. The nominal shear resisting area is 6.85 mm².

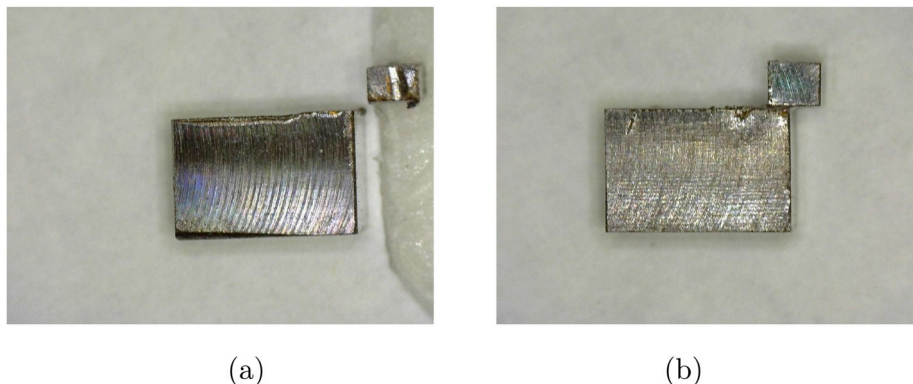


Fig. 4. Post-shear images for (a) as-welded/204 °C sample, and (b) HIP/204 °C sample.

Table 5

Area fraction of the failure features presented on the fracture surface.

Failure feature	as-welded/ 38 °C	HIP/ 38 °C	as-welded/ 204 °C	HIP/ 204 °C
Brittle failure	21.7%	7.7%	19.6%	1.5%
Machined surface	36.6%	N/A	N/A	N/A
Flow	27.4%	6.2%	3.9%	2.7%
Ductile failure	14.3%	86.1%	76.5%	95.8%

The standard deviation of shear strength for each condition is also given to characterize the variation of the shear test results. For the 204°C condition, the HIP process reduces the standard deviation from 13.57 MPa to 2.28 MPa. However, the results of the 38°C condition do not show the same trend, which needs further investigation. It is observed that the three loading curves of the HIP/38°C condition are not consistent with each other, which suggests that the HIP treatment has not healed all of the interfacial defects and brought interfacial properties of all three samples to the same level.

Slight increases in the shear strength and decreases in the standard deviation are found for as-welded structures when baseplate temperature increases from 38°C to 204°C. In similar fashion, the HIP/204°C condition has a higher shear strength and much lower standard deviation compared to the HIP/38°C condition. These results indicate that the increase of the baseplate temperature increases the shear strength of the bonding interface and improves consistency of the weld quality.

Images of typical post-shear test samples are provided in Fig. 4. The as-welded/204°C sample broke into two separate parts and the foil part of the sample was sheared off after a short loading displacement, while the HIP treated samples exhibited a higher resistance to shear and a more ductile failure mode.

The fracture surfaces of the post-shear UAM samples were examined by SEM. A manual point-count method [12] was used to quantify the fracture surface failure modes. Ten randomly located SEM images were taken for each treatment condition. Each SEM image was then evenly divided into 117 grids. Each grid was counted as one of four failure

features including machined surface, brittle failure, ductile failure, and flow. The area fraction of each failure feature for different treatment conditions is calculated and showed in Table 5. The definition for each failure feature is listed below and representative fracture surface images for different treatment conditions are shown in Fig. 5.

- Machined surface: Smooth surface area with small dark dots following the machining direction. Indicates no metallurgical bonding.
- Brittle failure: Sheared-off region with straight/sharp fracture.
- Ductile failure: Metallurgical bonding area with typical circular cup/cone type fracture normal to the fracture surface.
- Flow: Texture area produced by indentation of asperities. Indicates no metallurgical bonding but may provide mechanical interlocking.

Machined surface is the area where no bond was formed. Ductile failure represents the area where metallurgical bonding was formed during welding. Brittle failure and flow are the regions where mechanical interlocking is formed instead of metallurgical bonding. It is expected that mechanical interlocking is weaker than metallurgical bonding.

As shown in Table 5, a machined surface is only found for the as-welded/38 °C condition, which indicates a lack of plastic deformation at the welding interface. Compared with the as-welded/38 °C sample, as-welded/204 °C samples have larger ductile areas, smaller brittle and flow areas, and no machined surface, which means that higher baseplate temperature promotes metallurgical bonding at the welding interface. In addition, post-HIP samples exhibit larger ductile failure areas compared to as-welded samples, which indicates that further bond improvement is achieved with HIP. The results are consistent with the shear test results shown in Fig. 3. These fractured surface analyses, post-shear image examinations, and shear test results all suggest that a higher baseplate temperature and HIP treatment improve the mechanical strength and ductility of the UAM SS 410 weld interface.

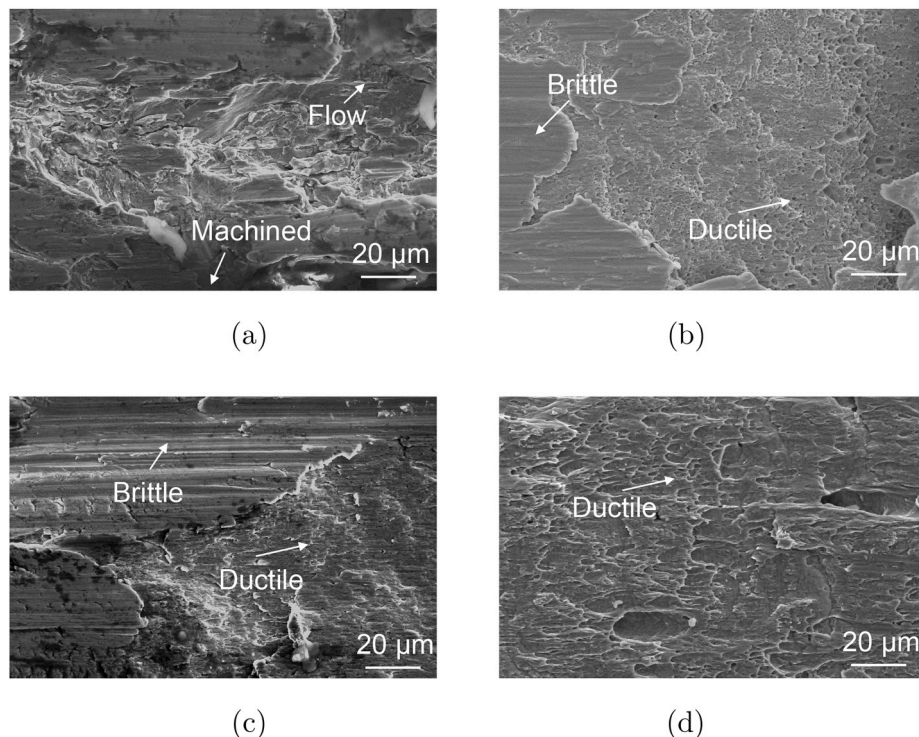


Fig. 5. SEM scans of the post-shear fractured surface of samples (a) as-welded/38 °C, (b) HIP/38 °C, (c) as-welded/204 °C, and (d) HIP/204 °C.

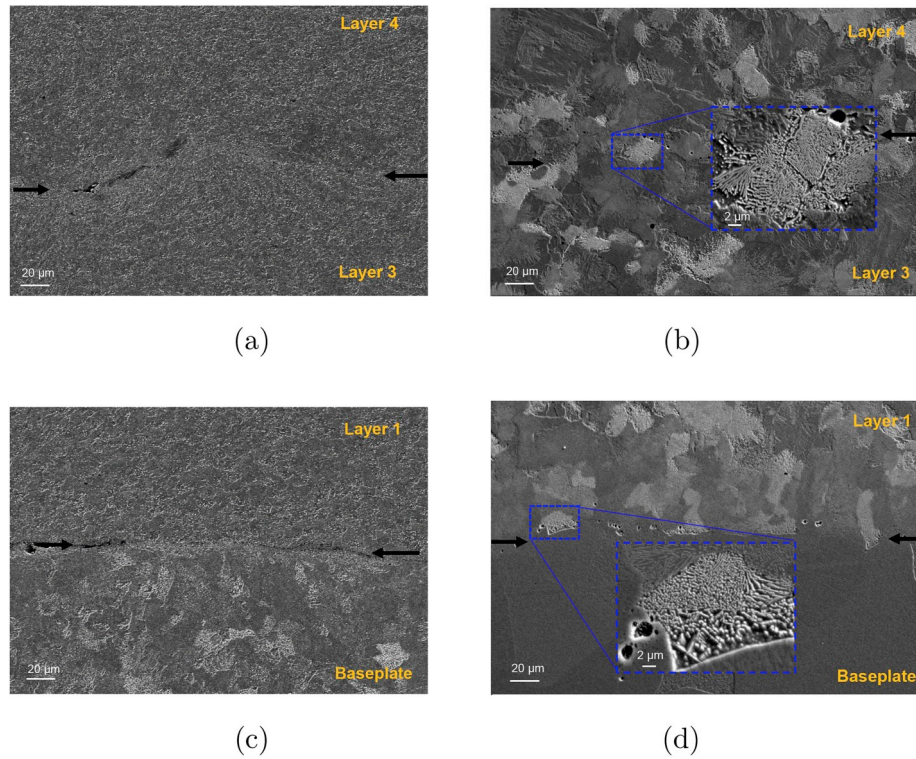


Fig. 6. Back-scattered electron micrographs of the UAM interfaces: (a) as-welded interface between the 3rd and the 4th layers of foil, (b) post-HIP interface between the 3rd and the 4th layers of foil, (c) as-welded interface between the baseplate and the 1st layer of foil, and (d) post-HIP interface between the baseplate and the 1st layer of foil.

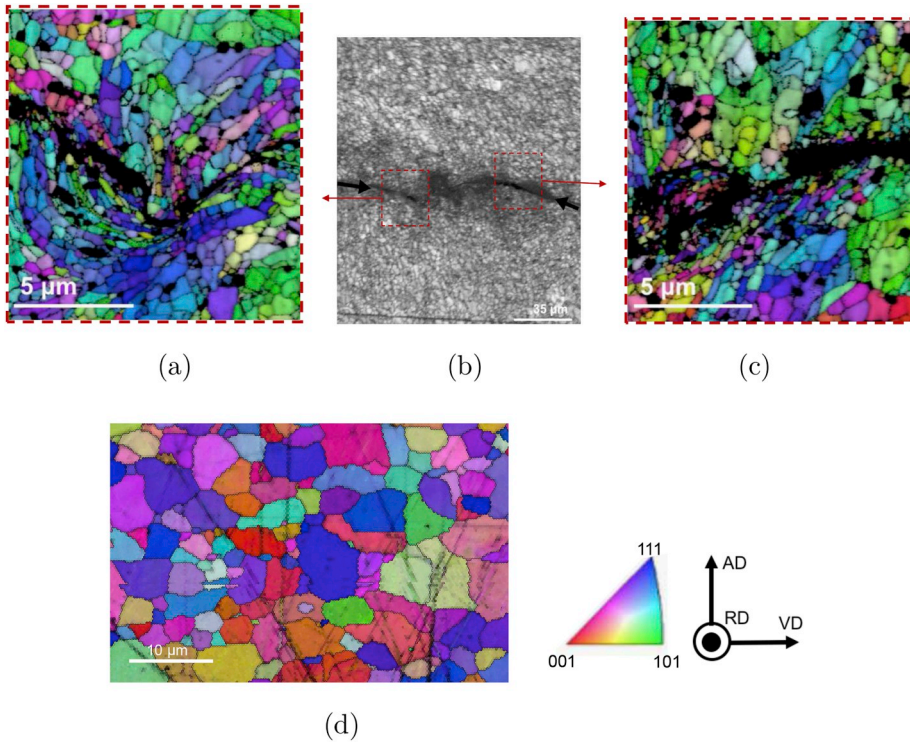


Fig. 7. EBSD micrographs of (a) bonded area, (b) UAM interface, (c) unbonded area, and (d) as-received SS 410 foil. The bonded areas are distinguished from unbonded areas by using SEM micrographs which are not shown here. Note that small black dots in (a) and (c) are not resolved due to small grains or distorted grains. The black distorted regions in the center part of (a) are black due to the significant plastic deformation resulting in the formation of zones with low image quality, while the black zones in the center part of (c) are voids.

3.2. Microstructural evaluations

3.2.1. Effect of baseplate temperature on microstructure of UAM SS 410

UAM SS 410 samples that were prepared at a baseplate temperature

of 204 °C were analyzed with SEM and EBSD. The back-scattered electrons (BSE) micrographs in Fig. 6(a) and (c) show that the interface (marked with black arrows) of as-welded UAM SS 410 predominantly consists of ferrite grains. Fig. 6(b) and (d) will be discussed in the next

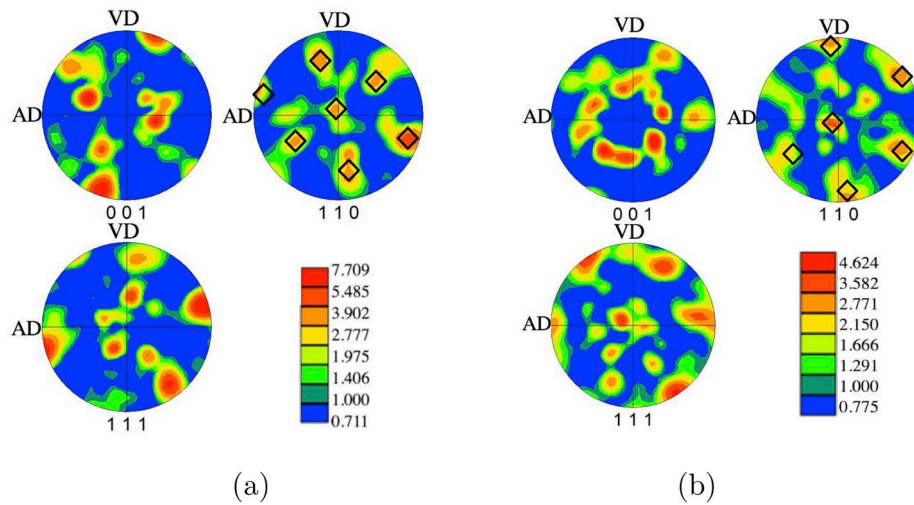


Fig. 8. Pole figures show identical alpha fiber texture indicating that BCC to FCC transformation did not occur during the UAM process; (a) micro texture of the unbonded area, and (b) micro texture of the bonded area.

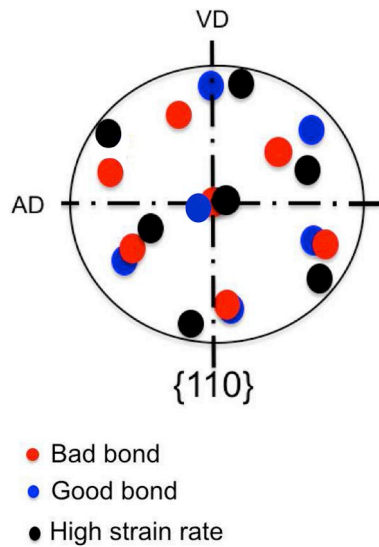


Fig. 9. Comparisons of the micro texture of the UAM bonded area, UAM unbonded area and high strain rate deformed interstitial-free steel [17].

section. EBSD micrographs of bonded and unbonded areas at the same UAM interface are shown in Fig. 7. The image quality mapping is shown in Fig. 7(b), while the inverse pole figure (IPF) is overlaid with the image quality mapping in Fig. 7(a) and (c). The coordinate system of the specimen is defined as the accumulating direction (AD), the vibrating direction (VD), and the rolling direction (RD) [21]. EBSD of the as-received 410 foil in Fig. 7(d) shows an equiaxed grain structure. Both bonded and unbonded areas at the interface appear to have highly deformed grains after the UAM process.

The micro texture presented in Fig. 8 shows the presence of a strong alpha fiber $\langle 110 \rangle \parallel \text{VD}$. Since no other variants, particularly Goss variants, are visible, the result suggests that the new grains do not occur from nucleation and growth, but evolve due to plasticity of the shear region [17]. As shown in Fig. 9, a similar alpha texture $\langle 110 \rangle \parallel \text{VD}$ is observed in the high strain rate deformed interstitial-free steel sample [17]. These similar texture patterns indicate that both the bonded and unbonded areas of the UAM interface may have experienced high strain rate deformation. The unbonded area is speculated to be a zone where excessive plastic deformation breaks the previously formed bonds.

3.2.2. Effect of HIP on microstructure of UAM SS 410

As discussed before, HIP increases the shear strength of UAM SS 410. To further investigate the influence of HIP on microstructure changes,

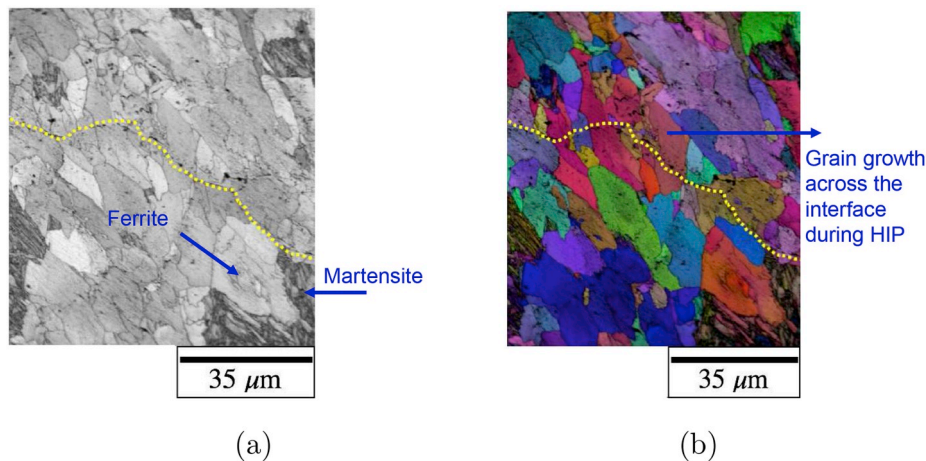


Fig. 10. EBSD micrographs of the UAM interfaces after HIP show a grain boundary migration across the interface. The IPF shows the presence of ferrite and local islands of martensite after HIP treatment; (a) image quality mapping, (b) image quality mapping overlapped with IPF.

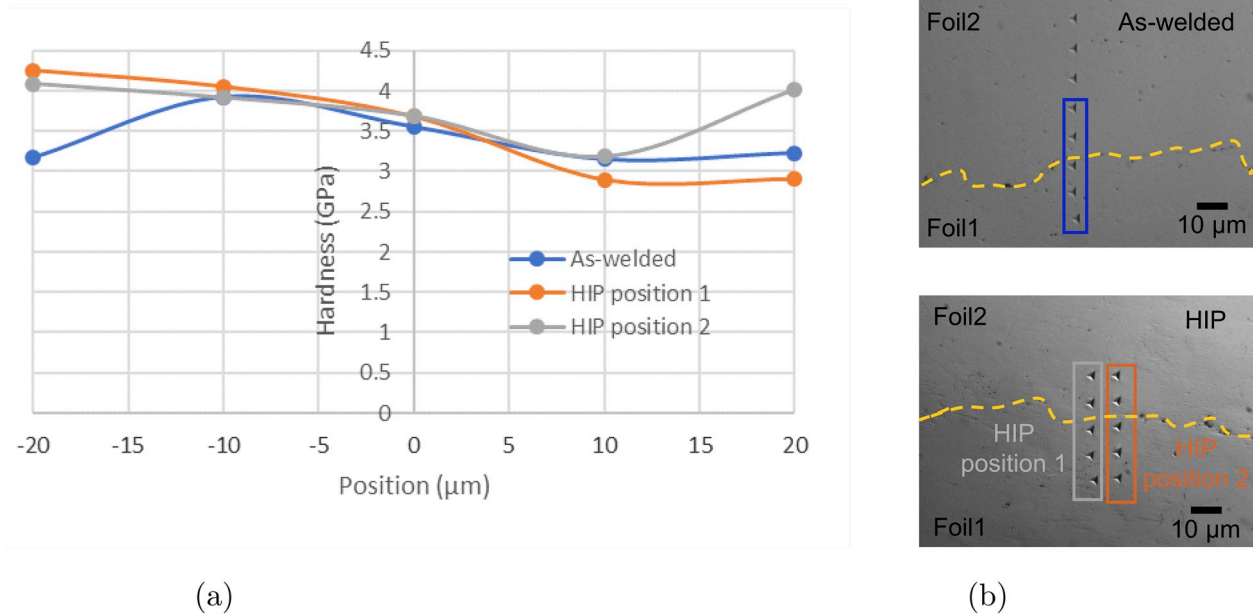


Fig. 11. (a) Nanoindentation hardness maps across the foil-foil interface (at zero μm) of the as-welded and post-HIP UAM samples, (b) corresponding indentation positions.

samples that were prepared at a baseplate temperature of 204°C were analyzed with SEM and EBSD. In the previous study on UAM of carbon steel 4130 [15], the UAM interfaces consist predominantly of only ferrite and the authors assume that the presence of nonmetallic inclusions at the interface results in the nucleation of ferrite and prevents the formation of pearlite. However, the interfaces of UAM SS 410 samples with HIP are composed of pearlite, as shown in Fig. 6(b) and (d). Additionally, the significant grain growth at the interface indicates that the pinning due to the oxides is a concern for Al but not for steel [22]. Due to the long exposure time and the slow cooling rates used in this study, the foil-to-foil interface is predominantly composed of pearlite as shown in Fig. 6(b) with some local pockets of martensite, which is determined by plate-like grains as shown in Fig. 10. The IPF is overlaid

on the image quality mapping and the interface is marked with a yellow dotted line. The baseplate-to-foil interface is mostly composed of pearlite. Microhardness tests were conducted in a grid pattern spanning across the sample thickness for cross sections of as-welded and HIP samples. The results show that due to the formation of the martensite, the overall hardness of the samples increased from 204 ± 7 HV in the as-welded condition to 240 ± 16 HV in the UAM with HIP condition. The entire cross section did not transform to martensite primarily due to the slow cooling rates of $2\text{--}4^\circ\text{C}/\text{min}$ in the HIP process.

3.2.3. Local mechanical properties characterization

To further investigate the microstructure changes during the UAM process, nanoindentation tests were performed to characterize the local hardness across the interface. As shown in Fig. 11, the top of layer n is harder than the bottom of layer $n+1$ for the as-welded UAM steel samples. The hardness of the top of layer n is increased because of severe plastic deformation which is due to the direct contact with the textured sonotrode. During the welding of layer $n+1$, the increased hardness in layer n is believed to limit the amount of plastic deformation and make it hard to collapse asperities, which may contribute to the formation of voids at the welding interface. The nanoindentation results also indicate that hardening is more pronounced at the interface. Since detailed microstructure characterization shows no evidence of a martensitic transformation, the increase in hardness at the interface is primarily due to grain boundary strengthening as reported previously [24].

The effect of HIP on the interfacial hardness is also investigated. The hardness around the post-HIP foil-to-foil interface is about 3.68 GPa, while the hardness around the as-welded foil-to-foil interface is about 3.55 GPa. The load vs displacement curves of as-welded and post-HIP samples show a similar trend in that the top of layer n is harder than the bottom of layer $n+1$. It is worth mentioning that the increase in hardness above the interface of some post-HIP regions is likely due to the indentation of a pocket of martensite, such as those shown in Fig. 10(a). The nanoindentation results of the selected regions are consistent with the microhardness results, which show that the post-HIP samples are harder than the as-welded samples.

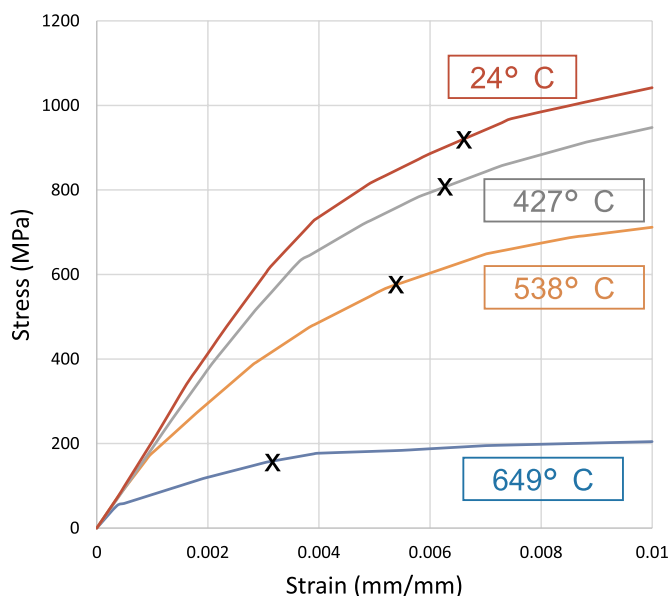


Fig. 12. Plots are regenerated based on the ASM atlas of stress-strain curves [18]. These stress strain curves are for SS 410 (371°C temper), which has a different heat treatment than the SS 410 used in this study.

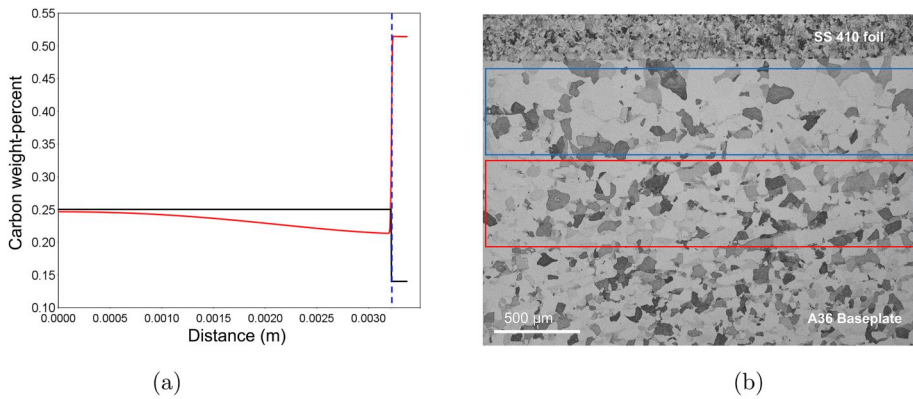


Fig. 13. (a) DICTRA simulation results: the black line represents the starting carbon content across the interface between the A36 steel baseplate and the SS 410, while the red line shows the ending carbon content. The blue dotted line represents the original interface. The left side is A36 baseplate and the right side is SS 410. (b) Optical image of the corresponding interface between the A36 baseplate and the SS 410 foil: dark areas are pearlite and light areas are ferrite. Area fraction of pearlite of two highlighted areas is calculated using ImageJ. Each highlighted area is $500\ \mu\text{m} \times 2519\ \mu\text{m}$. (For interpretation of the references to colour in this figure legend, the reader is referred to the web version of this article.)

4. Discussion

This study formally shows for the first time that increasing the baseplate temperature improves the interfacial strength of UAM SS 410. With higher baseplate temperatures and local temperature rise due to high strain rate deformation, the UAM interface temperature may exceed the critical temperature of BCC ferrite to FCC austenite phase transformation [4,11,17,27,29]. Since FCC austenite is relatively soft and easier to deform than BCC ferrite, further plastic deformation may be achieved for a given weld power condition, improving consolidation and corresponding bond quality. At a high enough cooling rate, as is the case in the UAM process [26], FCC austenite transforms into BCC martensitic grains. However, no martensitic phase is observed in as-welded material as shown in Fig. 6(a) and (c). The texture analysis results in Fig. 8 also indicate that the BCC ferrite to FCC austenite transformation did not occur, since no martensitic transformation texture was observed. It is therefore speculated that the improvement of UAM weld quality results from the reduction of yield strength with temperature (Fig. 12). Therefore, it becomes easier to deform asperities and to create metallurgical bonding of SS 410 at the interface. However, the exact reduction in yield strength is unknown since the interfacial temperature rise during welding of UAM SS 410 is unknown and difficult to measure locally. A future study is planned to measure and quantify the interfacial temperature rise.

HIP further improves the shear strength of UAM SS 410 to a level comparable to bulk SS 410. This improvement is attributed to the formation of a pearlite layer and the healing of interfacial defects at the interface between the A36 baseplate and the SS 410 foil. To form a fully pearlite layer, the amount of carbon at the interface has to exceed 0.76% (wt), while the starting amount of carbon in SS 410 foil is 0.14% (wt). It is hypothesized that this pearlite layer occurs as a result of carbon diffusion, which is driven by a carbon chemical potential difference. To evaluate the extent of carbon diffusion across the interface, DICTRA calculations have been performed as shown in Fig. 13(a). A 3.22 mm thick A36 steel and a 0.150 mm thick SS 410 foil are simulated in this 1D model. The black line shows the starting carbon content across the interface between the A36 steel baseplate and SS 410, while the red line shows the final carbon content. The interface position is marked with a blue dotted line. The results show that the carbon content of the A36 steel baseplate reduces from 0.25% to 0.21% (wt). The amount of carbon in the SS 410 side of the interface increases from 0.14% to 0.51% (wt). This uphill diffusion of carbon is caused by the high Cr concentration of SS 410 [2,33]. The calculated amount of carbon does not reach 0.76% (wt), but it is emphasized that the heating and cooling periods of the HIP process were not included for simplicity. In this DICTRA simulation, only the 4-h holding period of the HIP process is included. To validate the DICTRA simulation, an optical micrograph of a UAM SS 410 sample with HIP was analyzed using ImageJ software. As shown in Fig. 13(b),

dark areas are pearlite and light areas are ferrite. The area fraction of pearlite is calculated as 29.3% of the region highlighted with blue lines compared with an area fraction of 42.0% of the region highlighted with red lines. This shows a similar trend as the carbon content predicted by DICTRA.

5. Conclusions

Stainless steel 410 builds were fabricated using UAM. The mechanical properties of UAM SS 410 with HIP are comparable with those of bulk material. The study shows that increasing the baseplate temperature from 38°C to 204°C improves weld quality. HIP treatment improves the shear strength of UAM SS 410 samples by a factor of 2 as compared to as-welded UAM SS 410 samples. Post-shear fracture surface examinations reveal that as-welded/204°C samples have larger ductile failure areas than as-welded/38°C samples, which indicates that higher baseplate temperature promotes metallurgical bonding. Similarly, post-HIP samples have larger ductile failure areas than as-welded samples, which means that HIP further promotes metallurgical bonding. These analyses are consistent with shear test results. Further microstructural analyses of as-welded samples with SEM and EBSD show no evidence of BCC to FCC transformation taking place during the UAM process. The reduction of the yield strength of SS 410 at elevated temperature is believed to be the cause of weld quality improvement at higher baseplate temperature. A pearlite layer is found between the A36 baseplate and the first layer of SS 410 foil after HIP treatment. DICTRA simulations show that the pearlite layer occurs as a result of uphill carbon diffusion at the interface. HIP treatment is shown to increase the overall hardness of UAM SS 410 from 204 ± 7 HV to 240 ± 16 HV due to the formation of local pockets of martensite. Nanohardness tests show that the top of layer n is harder than the bottom of layer $n+1$. The increase in hardness at the interface is primarily due to grain boundary strengthening.

Acknowledgements

Financial support for this project is provided by the Government of Israel, Ministry of Defense PO No. 444080151. The authors want to thank Pressure Technology of Ohio, Inc. for performing the HIP treatments used in this study. Niyanth Sridharan wishes to acknowledge the U.S. Department of Energy, Office of Energy Efficiency and Renewable Energy, Advanced Manufacturing Office, Technical Collaborations Program. This manuscript has been authored by UT-Battelle, LLC under Contract No. DE-AC05-00OR22725 with the U.S. Department of Energy. The United States Government retains and the publisher, by accepting the article for publication, acknowledges that the United States Government retains a nonexclusive, paid-up, irrevocable, worldwide license to publish or reproduce the published form of this manuscript, or allow others to do so, for the United States Government purposes. The

Department of Energy will provide public access to these results of federally sponsored research in accordance with the DOE Public Access Plan (<http://energy.gov/downloads/doe-public-access-plan>).

Appendix A. Supplementary data

Supplementary data to this article can be found online at <https://doi.org/10.1016/j.msea.2019.138457>.

References

- [1] B. AlMangour, D. Grzesiak, J.-M. Yang, Selective laser melting of TiB₂/316L stainless steel composites: the roles of powder preparation and hot isostatic pressing post-treatment, *Powder Technol.* 309 (2017) 37–48.
- [2] A. Borgenstam, L. Höglund, J. Ågren, A. Engström, DICTRA, a tool for simulation of diffusional transformations in alloys, *J. Phase Equilibria* 21 (3) (2000) 269.
- [3] Z. Deng, M.B. Gingerich, T. Han, M.J. Dapino, Yttria-stabilized zirconia-aluminum matrix composites via ultrasonic additive manufacturing, *Compos. B Eng.* 115 (2018) 215–221.
- [4] R. Doherty, D. Hughes, F. Humphreys, J. Jonas, D.J. Jensen, M. Kassner, W. King, T. McNelley, H. McQueen, A. Rollett, Current issues in recrystallization: a review, *Mater. Sci. Eng. A* 238 (2) (1997) 219–274.
- [5] R. Gonzalez, B. Stucker, Experimental determination of optimum parameters for stainless steel 316L annealed ultrasonic consolidation, *Rapid Prototyp. J.* 18 (2) (2012) 172–183.
- [6] K. Graff, M. Short, M. Norfolk, Very high power ultrasonic additive manufacturing (VHP UAM) for advanced materials, in: *Solid Freeform Fabrication Symposium*, 2010 (Austin, TX).
- [7] H. Guo, M.B. Gingerich, L.M. Headings, R. Hahnlen, M.J. Dapino, Joining of carbon fiber and aluminum using ultrasonic additive manufacturing (UAM), *Compos. Struct.* 208 (2019) 180–188.
- [8] M. Gussev, N. Sridharan, Z. Thompson, K. Terrani, S. Babu, Influence of hot isostatic pressing on the performance of aluminum alloy fabricated by ultrasonic additive manufacturing, *Scr. Mater.* 145 (2018) 33–36.
- [9] R. Hahnlen, M.J. Dapino, NiTi-Al interface strength in ultrasonic additive manufacturing composites, *Compos. B Eng.* 59 (2014) 101–108.
- [10] A. Hehr, M.J. Dapino, Interfacial shear strength estimates of NiTi-Al matrix composites fabricated via ultrasonic additive manufacturing, *Compos. B Eng.* 77 (2015) 199–208.
- [11] J. Hines, K. Vecchio, Recrystallization kinetics within adiabatic shear bands, *Acta Mater.* 45 (2) (1997) 635–649.
- [12] C. Hopkins, P. Wolcott, M.J. Dapino, A. Truog, S. Babu, S. Fernandez, Optimizing ultrasonic additive manufactured Al 3003 properties with statistical modeling, *J. Eng. Mater. Technol.* 134 (1) (2012), 011004.
- [13] C. Kong, R. Soar, P. Dickens, Characterisation of aluminium alloy 6061 for the ultrasonic consolidation process, *Mater. Sci. Eng. A* 363 (1) (2003) 99–106.
- [14] C. Kong, R. Soar, P. Dickens, Optimum process parameters for ultrasonic consolidation of 3003 aluminium, *J. Mater. Process. Technol.* 146 (2) (2004) 181–187.
- [15] A. Levy, A. Miriyev, N. Sridharan, T. Han, E. Tuval, S. Babu, M.J. Dapino, N. Frage, Ultrasonic additive manufacturing of steel: method, post-processing treatments and properties, *J. Mater. Process. Technol.* 256 (2018) 183–189, 2018.
- [16] C.-H. Kuo, N. Sridharan, T. Han, M.J. Dapino, S. Babu, Ultrasonic additive manufacturing of 4130 steel using ni interlayers, *Sci. Technol. Weld. Join.* 24 (5) (2019) 382–390.
- [17] J. Lins, H. Sandim, H.-J. Kestenbach, D. Raabe, K. Vecchio, A microstructural investigation of adiabatic shear bands in an interstitial free steel, *Mater. Sci. Eng. A* 457 (1–2) (2007) 205–218.
- [18] C. Moosbrugger, *Atlas of Stress-Strain Curves*, ASM international, Ohio, 2002, p. 299.
- [19] L. Nickels, A new generation of HIP, *Met. Powder Rep.* 71 (3) (2016) 146–148.
- [20] J.J. Schomer, A.J. Hehr, M.J. Dapino, Characterization of embedded fiber optic strain sensors into metallic structures via ultrasonic additive manufacturing, in: *SPIE Smart Structures and Materials+ Nondestructive Evaluation and Health Monitoring*, International Society for Optics and Photonics, 2016, pp. 980320–980320.
- [21] S. Shimizu, H. Fujii, Y. Sato, H. Kokawa, M. Sriraman, S. Babu, Mechanism of weld formation during very-high-power ultrasonic additive manufacturing of Al alloy 6061, *Acta Mater.* 74 (2014) 234–243.
- [22] N. Sridharan, M.N. Gussev, C.M. Parish, D. Isheim, D.N. Seidman, K.A. Terrani, S. S. Babu, Evaluation of microstructure stability at the interfaces of Al-6061 welds fabricated using ultrasonic additive manufacturing, *Mater. Char.* 139 (2018) 249–258.
- [23] N. Sridharan, M. Gussev, R. Seibert, C. Parish, M. Norfolk, K. Terrani, S. Babu, Rationalization of anisotropic mechanical properties of Al-6061 fabricated using ultrasonic additive manufacturing, *Acta Mater.* 117 (2016) 228–237.
- [24] N. Sridharan, M. Norfolk, S.S. Babu, Characterization of steel-Ta dissimilar metal builds made using very high power ultrasonic additive manufacturing (VHP-UAM), *Metall. Mater. Trans. A* 47 (5) (2016) 2517–2528.
- [25] N. Sridharan, P. Wolcott, M.J. Dapino, S. Babu, Microstructure and texture evolution in aluminum and commercially pure titanium dissimilar welds fabricated using ultrasonic additive manufacturing, *Scr. Mater.* 117 (2016) 1–5.
- [26] M. Sriraman, S. Babu, M. Short, Bonding characteristics during very high power ultrasonic additive manufacturing of copper, *Scr. Mater.* 62 (8) (2010) 560–563.
- [27] J. Takahashi, K. Kawakami, M. Ueda, Atom probe tomography analysis of the white etching layer in a rail track surface, *Acta Mater.* 58 (10) (2010) 3602–3612.
- [28] R.B. Tuttle, Feasibility study of 316L stainless steel for the ultrasonic consolidation process, *J. Manuf. Process.* 9 (2) (2007) 87–93.
- [29] C. Wittman, M. Meyers, H.-R. Pak, Observation of an adiabatic shear band in AISI 4340 steel by high-voltage transmission electron microscopy, *Metall. Trans. A* 21 (2) (1990) 707–716.
- [30] P.J. Wolcott, M.J. Dapino, Ultrasonic additive manufacturing, in: *Additive Manufacturing Handbook: Product Development for the Defense Industry*, CRC Press/Taylor and Francis, Boca Raton, Florida, 2017.
- [31] P.J. Wolcott, A. Hehr, M.J. Dapino, Optimized welding parameters for Al 6061 ultrasonic additive manufactured structures, *J. Mater. Res.* 29 (17) (2014) 2055–2065.
- [32] P. Wolcott, N. Sridharan, S. Babu, A. Miriyev, N. Frage, M.J. Dapino, Characterisation of Al-Ti dissimilar material joints fabricated using ultrasonic additive manufacturing, *Sci. Technol. Weld. Join.* 21 (2) (2016) 114–123.
- [33] I. Wolf, H. Grabke, P. Schmidt, Carbon transport through oxide scales on Fe-Cr alloys, *Oxid. Metals* 29 (3–4) (1988) 289–306.
- [34] C.S. Zhang, A. Deceuster, L. Li, A method for bond strength evaluation for laminated structures with application to ultrasonic consolidation, *J. Mater. Eng. Perform.* 18 (8) (2009) 1124.